Is Bi2+ Responsible for the Red-Orange Emission of Bismuth-Doped SrB4O7?

5 AUTHORS, INCLUDING:

Andries Meijerink
Utrecht University

364 PUBLICATIONS   **13,582** CITATIONS

SEE PROFILE

Luis Seijo
Universidad Autónoma de Madrid

160 PUBLICATIONS   **3,827** CITATIONS

SEE PROFILE

Is Bi^{2+} responsible for the red-orange emission of bismuth-doped SrB$_4$O$_7$?

Mathijs de Jong,[1] Andries Meijerink,[1] Robert A. Gordon,[2] Zoila Barandiarán,[3, 4] and Luis Seijo[3, 4, *]

[1]*Condensed Matter and Interfaces, Debye Institute for Nanomaterials Science,*
Utrecht University, Princetonplein 5, 3584 CC Utrecht, The Netherlands
[2]*Pacific Northwest Consortium Synchrotron Radiation Facility, APS Sector 20, Argonne, IL, 60439, USA*
[3]*Departamento de Química, Universidad Autónoma de Madrid, 28049 Madrid, Spain*
[4]*Instituto Universitario de Ciencia de Materiales Nicolás Cabrera,*
Universidad Autónoma de Madrid, 28049 Madrid, Spain
(Dated: June 5, 2014)

Red-orange luminescence from bismuth-doped SrB$_4$O$_7$ has previously been reported and assigned to 6p-6p transitions of divalent Bi. To provide support for this assignment and the stability of this unusual valence state of Bi, we report here results from low temperature luminescence spectroscopy, X-ray absorption near-edge structure (XANES) spectroscopy, electron paramagnetic resonance (EPR) spectroscopy, and wave function based *ab initio* calculations. Low temperature luminescence spectra reveal zero-phonon lines (ZPLs) in excitation and emission spectra, allowing an accurate determination of the energies for the electronic transitions. The influence of the Bi-concentration on the emission intensity is shown to be small and only a small increase of the red-orange emission is observed upon raising the nominal Bi concentration from 0.02% (200 ppm) to 2%. This result indicates that only a very low concentration of Bi^{2+} can be incorporated in SrB$_4$O$_7$. This observation is supported by EPR experiments, which do not show a signal that can be assigned to Bi^{2+}, and XANES experiments showing that most Bi is in the trivalent state. An upper limit of the Bi^{2+} concentration is estimated to be 20 ppm. *Ab initio* calculations on the (BiO$_9$)$^{16-}$ cluster embedded in SrB$_4$O$_7$ give energies for excited states that are close to the experimentally observed energies. Also the luminescence life time for the red-orange emission ($\sim$12 μs) is consistent with the life time for 6p-6p emission calculated for the Bi^{2+} emission (3.5 μs). Equivalent *ab initio* calculations for Bi^{3+} luminescence are very far from the experimental results, providing independent evidence and additional support for the interpretation of stable Bi^{2+} species being responsible for the red-orange luminescence. The calculations provide a new interpretation of the third excitation band, which is not due to a $^2S_{1/2}$ state of the 6$s^2$7s configuration of Bi^{2+}, as previously assumed, but to a state with important characters of 6s6$p^2 - ^4P$ (63%) and doublets of the 6s6p^2, 6$s^2$6d, and 6$s^2$6p configurations; its higher intensity is due to its character of parity allowed 6$s \rightarrow$ 6p and 6$p \rightarrow$ 6d excitations.

Keywords: EPR, XANES, luminescence, *ab initio*, bismuth, Bi^{2+}, SrB$_4$O$_7$, phosphor, 6$p_{1/2} - 6p_{3/2}$ splitting

I. INTRODUCTION

Divalent bismuth is rarely reported in inorganic chemistry textbooks. It was not until 1994 that the Bi^{2+} species was considered to be stable by Blasse *et al.*[1] and to be responsible for the red-orange luminescence of bismuth activated SrB$_4$O$_7$. By extension, Bi^{2+} was assumed to cause the red luminescence of bismuth activated alkaline earth sulfates already reported in 1886 by De Boisbaudran[2] and of bismuth activated phosphates reported in 1949 by Kröger *et al.*[3] (cf. Ref. 4). Recently, this ion has motivated a new approach in the search of new phosphors for energy efficient solid-state lighting devices and several reports on bismuth activated luminescent materials have been published which assumed Bi^{2+} as the active species.[5–11] This assumption was mainly supported on arguments that justify that the excitation and emission energies and the excited state lifetime could not be explained by the participation of any other bismuth species but Bi^{2+}.

In effect, the emission band and two excitation bands in the 17000 and 21000 cm^{-1} regions in borates, sulfates, and phosphates have been interpreted as due to local states associated with the spin-orbit $^2P_{1/2}$ and $^2P_{3/2}$ levels of the 6$s^2$6p configuration of Bi^{2+}, the latter split under low symmetry fields into $^2P_{3/2}$(1) and $^2P_{3/2}$(2) levels.[1,5,8] These are

6$p \rightarrow$ 6p parity forbidden transitions in the free-ion that become allowed in the host by the effect of the low symmetry fields. A higher energy, more intense excitation band in the 40000 cm^{-1} region (also observed in bismuth doped alkaline earth fluorides[11]) is attributed in all cases to a 6$p \rightarrow$ 7s transition: 6$s^2$6$p - ^2P_{1/2} \rightarrow$ 6$s^2$7$s - ^2S_{1/2}$. The fact that this is a parity allowed transition in the free-ion would explain its higher intensity.

While Bi can be found in compounds with formal valence ranging from -3 to +5, with even non-integral valencies possible (*e.g.* in cluster compounds)[12,13], there is, however, little evidence for the existence of stable Bi^{2+} active centers in solids, apart from the optical spectroscopy measurements.

In this paper, we report results of several techniques aimed at clarifying the existence of a Bi^{2+} active center in bismuth-doped crystalline SrB$_4$O$_7$ and the assignment of the red-orange luminescence of this material.

We show experimental results of low temperature excitation and emission spectra, XANES measurements, and 20 K EPR measurements. We also show *ab initio* calculations on the electronic structure of Bi^{2+} as a free-ion and as a substitutional defect in SrB$_4$O$_7$. XANES and EPR do not give signals from Bi^{2+}. Luminescence experiments that supplement older measurements[1] detect the zero-phonon lines of

$^2P_{3/2}(1)$ and $^2P_{3/2}(2)$ and indicate that the concentration of the red emitter is very low. *Ab initio* calculations provide details of energies, lifetimes, and the nature of the Bi^{2+} electronic states, as well as transition oscillator strengths. The overall agreement between the electronic structure of these states and the optical spectroscopic experiments provides strong support for the existence of Bi^{2+} and to the general interpretation of its luminescence. A new interpretation is provided for the third excitation to a higher state in the 40000 cm^{-1} region, which is found to be a configuration interaction mix of $6s \rightarrow 6p$, $6p \rightarrow 6d$, and $6p \rightarrow 7p$ excitations rather than a $6p \rightarrow 7s$ transition.

The luminescence experiments are discussed in Sec. II, the XANES experiments in Sec. III, the EPR experiments in Sec. IV, and the *ab initio* calculations in Sec. V. The conclusions are presented in Sec. VI.

II. LUMINESCENCE

A. Method

Bismuth-doped SrB_4O_7 was prepared as described by Blasse *et al.*[1] Stoichiometric amounts of $SrCO_3$, H_3BO_3 and Bi_2O_3 for 0.02 %, 0.4 % and 2 % bismuth concentrations were mixed and fired in N_2 atmosphere first at 450°C for 2 hours and a second time at 840°C for 8 hours. Firing in reducing atmosphere (H_2) yielded non-luminescent SrB_4O_7. Higher firing temperatures resulted in a glass material.

Luminescence spectra were recorded using an Edinburgh FLS920 spectrofluorometer with a 450W xenon lamp as excitation source and a Hamamatsu R928 PMT as detector. For the low temperature measurements the spectrofluorometer was equipped with an Oxford Instruments helium cryostat. The decay times were measured using an Opotek Opolette 355 tunable laser in combination with the FLS920 spectrofluorometer, a Hamamatsu H7422-02 PMT and a EG&G Ortec Turbo-MCS.

B. Zero-phonon lines

The 4.2 K excitation and emission spectra of bismuth-doped SrB_4O_7 are shown in Fig. 1. Sharp zero-phonon lines are visible in the emission spectrum and in the two first bands of the excitation spectrum. Although the excitation and emission spectra of this material have been measured before,[1,7] the energies of the zero-phonon lines have not been reported. Precise values of 17245 cm^{-1} and 20705 cm^{-1} (Table I) are found for the $^2P_{1/2} \leftrightarrow {}^2P_{3/2}(1)$ and $^2P_{1/2} \rightarrow {}^2P_{3/2}(2)$ transitions, respectively.

The fine structure of the excitation band at high energy could not be resolved and the energy level of this higher excited state is therefore chosen as the maximum of this excitation band. The integrated excitation intensity, which is a product of the absorption strength and the quantum efficiency for luminescence resulting from the excitation, was

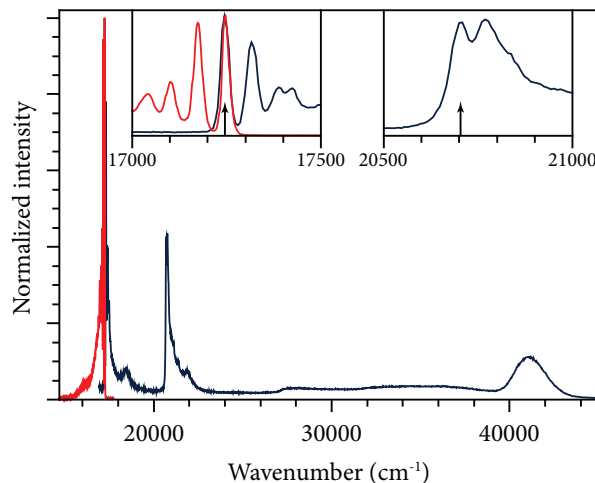obtained by integrating the excitation bands in the spectrum. The values are listed in Table I.

FIG. 1: Low temperature (4.2 K) excitation spectrum (blue line, emission at 620 nm) and emission spectrum (red line, excitation at 480 nm) of SrB_4O_7 doped with 0.02 % bismuth. Spectra are corrected for the intensity of the lamp in combination with the excitation monochromator and for the detector sensitivity in combination with the emission monochromator. The spectrum was converted from wavelength to energy scale, including the correction for the spectral distribution. The insets show in more detail the parts of the spectrum where the zero-phonon lines of the $^2P_{1/2} \leftrightarrow {}^2P_{3/2}(1)$ transitions (left inset) and $^2P_{1/2} \rightarrow {}^2P_{3/2}(2)$ transition (right inset) are located.

TABLE I: Experimental energy levels, in cm^{-1}, and integrated excitation intensities relative to $^2P_{1/2} \rightarrow {}^2P_{3/2}(1)$.

Level [a]	Main character [a]	Energy	Excitation intensity
$1E_{1/2}$	$^2P_{1/2}$	0	
$2E_{1/2}$	$^2P_{3/2}(1)$	17245 (ZPL)	1.00
$3E_{1/2}$	$^2P_{3/2}(2)$	20705 (ZPL)	0.98
$4E_{1/2}$	63% ^4P	41100 (max)	1.38

[a]This work assignment (cf. Sec. V).

C. Concentration dependence

An analysis of the dependence of the emission intensity on the bismuth concentration reveals more about the incorporation of the bismuth in a divalent state in the SrB_4O_7 lattice. For three concentrations of bismuth, an emission spectrum is shown in Fig. 2. While there is a large variation in the bismuth concentrations in the starting material (from 0.02% to 2% there is a 100-fold increase), the emission intensity only varies slightly (from 0.02% to 2% there is a 2.3-fold increase).

To investigate whether a quenching effect plays a role at higher bismuth concentrations, time-resolved emission
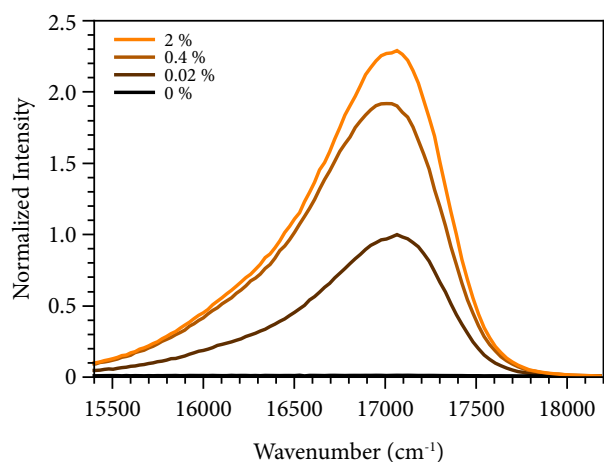
FIG. 2: Emission spectra for a variety of bismuth doping concentrations of in SrB_4O_7. The spectra are normalized to the emission maximum of the 0.02% doped material. While there is a 100-fold increase in bismuth concentration in the starting mixture of the synthesis for the samples with 0.02% and 2% bismuth, there is only a 2.3-fold increase in emission intensity.

measurements were done. The emission showed a mono-exponential decay, shown in Fig. 3. There is only a small decrease in the decay time at higher concentrations, which cannot explain the limited increase of emission intensity as a concentration quenching effect.
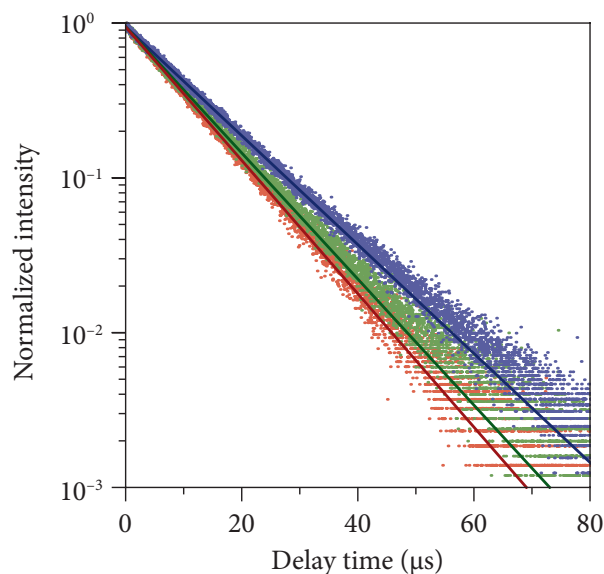

FIG. 3: Emission decay curves of 0.02 % (blue), 0.4 % (green) and 2 % (red) bismuth doped SrB_4O_7. The decay times corresponding to the mono-exponential fits are respectively 12.3 μs, 10.7 μs and 10.1 μs.

From the integrated emission intensities and the emission decay times it can be concluded that upon increasing the bismuth concentration in the synthesis starting mixture, only a small fraction of this bismuth ends up in the SrB_4O_7

lattice in a divalent state. This is in line with the knowledge that 2+ is not a stable oxidation state for bismuth, unlike 3+ and 5+. This suggests that also at 0.02% doping concentration only a part of the bismuth is incorporated as Bi^{2+} and that the concentration of the Bi^{2+} ion in our experiments is possibly much lower than 0.02% (200ppm).

III. XANES EXPERIMENTS

A. Method

X-ray Absorption Near-Edge Structure (XANES) spectroscopic measurements at the Bi LIII edge were performed at beamline 20BM (PNC/XSD) at the Advanced Photon Source (APS). Incident X-rays from a Si(111) double-crystal monochromator were either toroidally focused to a spot size of 500 by 400 μm^2 (0.02% doping sample) or unfocused (2% and Bi_2O_3 reference). For focused-mode, a 0.3 mm high white beam slit 25 m from the bending magnet source was used, versus 0.5 mm high for unfocused mode with sample slit height 0.9 mm at 50 m from the source. The X-ray monochromator was detuned to 80% of the maximum signal at 13.700 keV and a Rh-coated planar mirror at 3.5 mrad angle also used for harmonic rejection. Fluorescent X-rays were monitored using a 12-element Germanium detector (Canberra): transmission ion chambers (N_2-filled) for transmission. A 10 μm thick Bi foil (Goodfellow) was used to monitor energy calibration after the sample-transmission ion chamber. Samples were measured as pellet (0.02% doped), packed powder (2%) or powder on kapton tape (Bi_2O_3, 8-layers, measured in transmission).

B. Bismuth oxidation states in SrB_4O_7

XANES spectra for 0.02% and 2% doped SrB_4O_7, along with reference Bi metal foil and Bi_2O_3 are overlaid in Fig 4. Background removal and normalization to unit edge step were done using the programme WinXAS.[14] Compared to the foil, the trivalent oxide reference exhibits a shift to higher binding energy in absorption, where the reduced 6p valence electron occupation reduces the screening of the core 2p and valence 6d states from the nuclear charge. A pronounced difference in structure is evident between the oxide and 0.02%-doped data. Different local Bi environments can cause such changes.[15] The 2%-doped sample has features reminiscent of both the oxide and 0.02%-doped samples, suggesting the sample is mixed-phase and the doping level is only nominally 2% based on the starting level, not the end product.

Considering the 0.02% result in more detail, we note that the edge position for this sample is comparable to that for the trivalent oxide. This is strongly suggestive that the dominant contribution to the XANES is from a trivalent Bi species. If the dominant Bi species were divalent, one
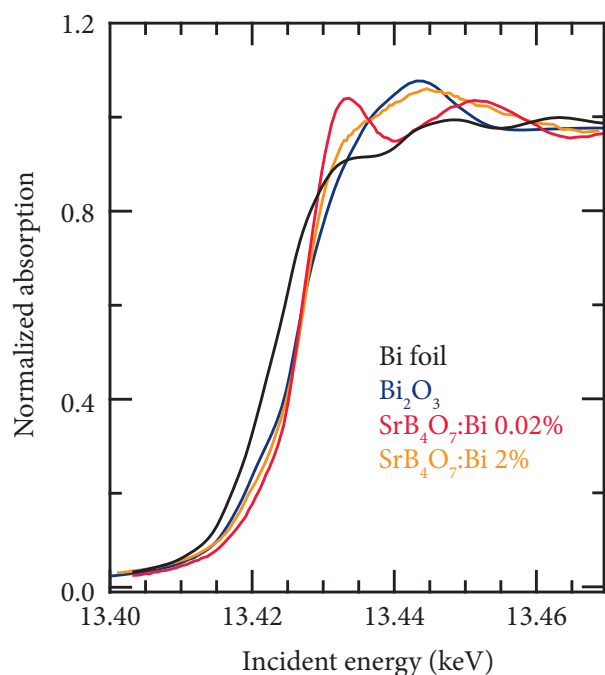
FIG. 4: Comparision of normalized XANES spectra for 0.02% and 2% bismuth-doped SrB_4O_7, with reference spectra for Bi foil and Bi_2O_3.

would expect the presence of a 6p valence electron to correlate with a smaller edge shift from the Bi metal foil position. For this reason only a fraction of the 200 ppm bismuth could be in a divalent state, below detection levels for this method. An upper limit of 20 ppm Bi^{2+} is estimated. For more than 10 % of Bi in the divalent state, a shift of the edge should be observable. This is consistent with the effects of concentration of starting material on luminescence intensity.

The Bi-dopant concentration dependence of the XANES spectrum allows us to make a comment on the incorporation of Bi^{3+} in the SrB_4O_7 lattice. We note the reduction in amplitude in the region just above the absorption onset, between 13.420 and 13.425 keV and interpret such as a reduction in covalent interactions between Bi and O in the borate versus the oxide. If, as the XANES indicates, the Bi is entering the SrB_4O_7 structure as a predominantly trivalent species, with B^{3+} substantially smaller than $Bi^{3+}$and Sr^{2+}slightly larger[16], occupation of a Sr site is more probable. Charge balance would dictate that for every two substitutions, either an additional Sr vacancy must also be created, or another anion - interstitial oxygen - be present. Either of these mechanisms could lead to a destabilizing of the structure and lead to the limit in incorporation of Bi^{3+} observed in the nominal 2% doped sample. In considering what the doping limit may be, we compared linear combinations of the 0.02% doped SrB_4O_7 (assumed only to be from substitution) and Bi_2O_3 XANES spectra to the 2% doped SrB_4O_7 XANES spectrum and found the best agreement between ratios 30:70 and 40:60 for 0.02% doped

SrB_4O_7 : Bi_2O_3. The XANES spectra therefore suggest that the limit of Bi^{3+} incorporation is at most 0.6 - 0.8%.

IV. EPR EXPERIMENTS

An unpaired electron in an atomic orbital gives an ion a magnetic moment, which gives rise to an energy difference between the two possible orientations of the magnetic moment in a magnetic field. Electron paramagnetic resonance (EPR) spectroscopy makes use of this splitting and this technique can prove the presence of unpaired electrons. The $6s^26p$ ground state of Bi^{2+} has a single electron in a 6p-orbital and the energy gap between the two orientations of the spin of this electron in the magnetic field can be measured.

For Bi^{2+} bismuth this experiment was first done by Murphy *et al.*[17] They used a bismuth doped $CdWO_4$ crystal and measured an X-band EPR spectrum at 27 K after the material was irradiated with X-rays at 77 K. No EPR signal was observed before irradiation. The observed signal consists of peaks at $g = 1.543$, $g = 1.380$ and $g = 1.623$ for the three different crystallographic axes, split up in ten components, which is expected from the coupling of the unpaired electron to the $I = \frac{9}{2}$ nuclear spin of ^{209}Bi. It was necessary to keep the crystal at low temperature between irradiation with X-rays and the EPR experiment. This indicates that the Bi^{2+} ion in $CdWO_4$ is not stable at room temperature.

According to our optical spectroscopy measurements, Bi^{2+} in SrB_4O_7 is stable at room temperature in low concentrations. EPR measurements on non-irradiation-induced Bi^{2+} have not been reported before, therefore an attempt was made to measure the unpaired electron in SrB_4O_7:Bi^{2+} at room temperature.

Both room temperature, 20 K and 40 K measurements were performed using a Bruker EPR spectrometer in the X-band (9.4 GHz). SrB_4O_7 powders with bismuth dopant concentrations of 0.02 %, 0.4 % and 2 % were used. At room temperature none of them showed any signal in the region from 0 to 1.6 T. At 20 K and 40 K only low concentrations of iron impurities were observed in a scan from 0 to 0.6 T, but no signal belonging to bismuth was recorded, even though Bi^{2+} should in principle be observable in this region, as proven by Murphy *et al.*[17] Since EPR is a very sensitive technique, it indicates that if bismuth is present in a divalent state, this must be below the level of sensitivity of the measurement, similar to the XANES experiments.

V. AB INITIO CALCULATIONS

A. Method

We performed *ab initio* wave function theory embedded cluster quantum chemical calculations on the $(BiO_9)^{16-}$ cluster embedded in the SrB_4O_7 host with the MOLCAS suite of programs.[18] They include Bi-O bonding effects, static and dynamic electron correlation effects, and scalar

and spin-orbit coupling relativistic effects within the cluster, as well as Coulomb, exchange, and Pauli repulsion embedding effects from the host onto the cluster. Electron correlation effects between the cluster and the host are excluded from these calculations. Since Bi subsitutes for Sr in SrB_4O_7 and Sr occupies a C_s point symmetry site,[19] most of the calculations have been performed using this symmetry, except for structures with Bi off-plane, where C_1 symmetry was used instead.

The embedded cluster calculations are two-step spin-orbit coupling SA-CASSCF/MS-CASPT2/RASSI-SO DKH calculations. In the first step, we used the many-electron scalar relativistic second-order Douglas-Kroll-Hess (DKH) Hamiltonian.[20,21] We performed state-average complete-active-space self-consistent-field[22–24] (SA-CASSCF) calculations with the active space that results from distributing 3 electrons in 13 active molecular orbitals with main character Bi $6s$, $6p$, $6d$, $7s$, and $7p$: $[6s, 6p, 6d, 7s, 7p]^3$. In C_s symmetry the active space is $[9 \times a', 4 \times a'']^3$. In the SA-CASSCF calculations, the following energy averages were minimized: The average of 17 states derived from the lowest doublets of free Bi^{2+} ($6s^2 6p -{}^2 P^o$, $6s^2 7s -{}^2 S$, $6s^2 6d -{}^2 D$, $6s 6p^2 -{}^2 P$, $6s 6p^2 -{}^2 D$) and the average of the 3 states derived from the term $6s 6p^2 -{}^4 P$ of Bi^{2+}. In C_s symmetry, this means the independent averages of the first 11 $^2 A'$, 6 $^2 A''$, 2 $^4 A'$, and 1 $^4 A''$ states. The SA-CASSCF calculations provided occupied and empty molecular orbitals to feed subsequent multi-state second-order perturbation theory calculations (MS-CASPT2),[25–28] where the dynamic correlation of 85 electrons (the $5d, 6s, 6p$ electrons of Bi and $2s, 2p$ electrons of the nine O atoms) were taken into account. We used the standard IPEA value (0.25 au).[29]

In the second step, we included spin-orbit coupling effects by adding the AMFI approximation of the DKH spin-orbit coupling operator[30] to the scalar relativistic Hamiltonian. In this step, we used the spin-free-state-shifting operator as a means to combine spin-orbit couplings calculated with statically correlated wave functions and spin-orbit free energies calculated with dynamic correlation[31] and, accordingly, we performed restricted-active-space state-interaction spin-orbit calculations (RASSI-SO)[32,33] with the transformed CASSCF wave functions (first-order wave functions of the MS-CASPT2 method) and the MS-CASPT2 energies. We allowed the mixing of the first 17 doublets and 3 quartets. In C_s symmetry they are 1-11 $^2 A'$, 1-6 $^2 A''$, 1-2 $^4 A'$, and 1 $^4 A''$, and they give 23 $E_{1/2}$ Kramers doublets. We also performed some calculations on the corresponding embedded cluster of Bi^{3+}, $(BiO_9)^{15-}$, for comparisons. For these, we used the active space that results from distributing 2 electrons in 4 active molecular orbitals with main character Bi $6s$ and $6p$: $[6s, 6p]^2$ and we computed the singlets and triplets related with the atomic $6s^2 -{}^1 S$, $6s 6p -{}^1 P^o$, and $6s 6p -{}^3 P^o$, and the spin-orbit coupling between them.

All the calculations are all-electron, with atomic natural orbital (ANO) relativistic basis sets for bismuth and oxygen,[34] with respective contractions $(25s22p16d12f4g)/[11s10p9d6f4g]$ and

$(14s9p4d)/[4s3p2d]$.

The Hamiltonian of the $(BiO_9)^{16-}$ cluster was supplemented with the AIMP embedding potential[35] of SrB_4O_7, which has been obtained in this work. It is available from the authors[36] and presented in the supplementary material. This embedding potential is made of: 1) total-ion embedding AIMPs representing Sr^{2+} and B^{3+} cations and O^{2-} anions, which are located at experimental sites of the SrB_4O_7 lattice, within a cube made of $3 \times 3 \times 3$ unit cells and centered on Sr^{2+}, and 2) a set of 16584 additional point charges situated at lattice sites, generated by the zero-multipole method of Gellé and Lepetit,[37] which closely reproduce the Ewald potential[38] within the cluster. The experimental crystal structure of SrB_4O_7 (Ref. 19) is the following: Space group number 31, $Pmn2_1$ orthorhombic; lattice constants $a=10.711$ Å, $b=4.427$ Å, $c=4.235$ Å; 2(a) sites occupied by Sr ($y_{Sr}=0.289$, $z_{Sr}=0$) and O_1 ($y_{O_1}=0.728$, $z_{O_1}=0.454$) and 4(b) sites occupied by O_2 ($x_{O_2}=0.359$, $y_{O_2}=0.857$, $z_{O_2}=0.064$), O_3 ($x_{O_3}=0.221$, $y_{O_3}=0.631$, $z_{O_3}=0.335$), O_4 ($x_{O_4}=0.365$, $y_{O_4}=0.226$, $z_{O_4}=0.335$), B_1 ($x_{B_1}=0.379$, $y_{B_1}=0.174$, $z_{B_1}=0.976$), and B_2 ($x_{B_2}=0.246$, $y_{B_2}=0.671$, $z_{B_2}=0.936$). The embedding AIMPs have been obtained in self-consistent embedded-ions (SCEI)[39] Hartree-Fock (HF) calculations.

B. Electronic structure of Bi^{2+} free-ion

It is interesting to know the performance of the present *ab initio* method in the Bi^{2+} free-ion because its electronic states are a reference for the states of Bi^{2+} in SrB_4O_7 and other solids.

In free Bi^{2+} we performed the same type of SA-CASSCF/MS-CASPT2/RASSI-SO DKH calculations as in the $(BiO_9)^{16-}$ cluster. We used the same basis set, active space, and dynamic correlation described in Sec. V A. For methodological convenience, we used C_i symmetry. We used even weights for the states of separated SA-CASSCF calculations in: $^2 L^o$ *odd* terms $6s^2 6p -{}^2 P^o$ and $6s^2 7p -{}^2 P^o$; $^2 L$ *even* terms $6s^2 7s -{}^2 S$, $6s^2 6d -{}^2 D$, and $6s 6p^2 -{}^2 P$, $^2 D$, and $^2 S$; and $^4 L$ *even* term $6s 6p^2 -{}^4 P$. Note that the states are multiconfigurational and only the main configurational characters are indicated. The results are shown in Table II in the column labeled "Even SA weights". We can observe a rather good agreement with the experimental energies[40] in all states under consideration, with a root mean square deviation of 2380 cm^{-1} in transitions starting in 20000 cm^{-1} and going as high as 130000 cm^{-1}, and a $6s^2 6p -{}^2 P^o$ spin-orbit splitting of 18811 cm^{-1}, which underestimates the experiment 9.5%.

Such underestimation of the spin-orbit splitting is in line with a 15% underestimation of the splitting in Tl obtained in spin-orbit configuration interaction (SOCI) calculations[41] and it is related to the fact that the $6p_{1/2}$ and $6p_{3/2}$ spinors are not optimized with a spin-orbit Hamiltonian. In our calculations, the differences in the radial functions of these spinors result only from the orbital excitations considered in the configuration interaction step with the spin-

orbit coupling Hamiltonian, so that when this difference is as large as in 6p elements the CI may be insufficient. In these cases, jj-coupling based methods perform especially better than LS-coupling based methods like the present one.[41] It is interesting to observe that in Bi^{2+}, the configuration interaction between $6s^26p-{}^2P^o$ and $6s^27p-{}^2P^o$ allows to obtain different $6p_{1/2}$ and $6p_{3/2}$ spinors via mixing of the

6p orbital with the 7p orbital in the so-called double-shell effect.[42,43] So, we explored here to what extent the different 6p-7p mixings resulting from using different state-average weights of the $6s^26p-{}^2P^o$ and $6s^27p-{}^2P^o$ states in the SA-CASSSCF calculation can affect the ${}^2P^o$ spin-orbit splitting.

TABLE II: Experimental and calculated spectra of Bi^{2+} free-ion. Results of two calculations with different choices of state-average weights are shown; see text for details. Energies in cm^{-1}. Deviations from experiments are shown in parentheses.

Main configuration	Term	J	Experiment[a]	This work	
				Even SA weights	1-4 SA weights
$6s^26p$	${}^2P^o$	1/2	0	0	0
		3/2	20788	18811 (−1977)	20345 (−443)
$6s6p^2$	${}^4P$	1/2	70254	73654 (+3400)	73406 (+3152)
		3/2	83038	83416 (+378)	83876 (+838)
		5/2	89236	88979 (−257)	88722 (−514)
$6s^27s$	${}^2S$	1/2	95075	93875 (−1200)	94404 (−671)
$6s^26d$	${}^2D$	3/2	96154	95082 (−1072)	94397 (−1757)
		5/2	102446	99834 (−2612)	101101 (−1345)
$6s6p^2$	${}^2P$	1/2	108052	108222 (+170)	109200 (+1148)
		3/2	130966	127230 (−3736)	127651 (−3315)
$6s6p^2$	${}^2D$	3/2	108586	105595 (−2991)	105550 (−3036)
		5/2	116414	112370 (−4044)	111333 (−5081)
$6s^27p$	${}^2P^o$	1/2	116993	115477 (−1516)	117045 (+52)
		3/2	122128	119846 (−2282)	121240 (−888)
$6s6p^2$	${}^2S$	1/2	130986	128275 (−2711)	129488 (−1498)
	rms deviation			2379	2158
Bi^{3+} $6s^2$	${}^1S$	0	206180	203463 (−2717)	204748 (−1432)

[a]Reference 40.

In Table II (column "1-4 SA weights") we show the results of using relative weights of 1 and 4, respectively, for the states of the $6s^26p$ and $6s^27p$ configurations of the ${}^2P^o$ block. Although less relevant for the ${}^2P^o$ spin-orbit splitting, we also used relative weights of 1 for $6s^27s-{}^2S$, $6s^26d-{}^2D$, and $6s6p^2-{}^2P$, ${}^2D$, and ${}^2S$, and 4 for two additional ${}^2P$, two ${}^2D$, and two ${}^2S$ terms of the $6s6p7p$ configuration. We can see that the different 6p-7p mixings in the $6p_{1/2}$ and $6p_{3/2}$ spinors that result in this case improve the ${}^2P^o$ spin-orbit splitting, reducing its underestimation of experiment to 2.1%. However, we must bear in mind that using this technique as a means to improve the 6p related spinors of Bi^{2+} in solids demands averages of the $6s^26p-{}^2P^o$ related states with $6s^27p-{}^2P^o$ related states, which are very high in energy. This becomes impractical when the inversion center is lost, as in SrB_4O_7:Bi^{2+}, because a large number of $6s^26d$, $6s^26s$, and $6s6p^2$ related states are inserted between the target states of the state-average.

C. Electronic structure of Bi^{2+} in SrB_4O_7

In this Section we show the computed energy levels of the $(BiO_9)^{16-}$ cluster embedded in SrB_4O_7. The results correspond to the (ground and excited states) cluster structures resulting after the off-center relaxation of the position of Bi^{2+} within the rigid O_9 cage created by the stiff oxygen network of the diborate, which was made in Ref. 44 at the spin-orbit coupling level of calculation. Bi^{2+} was found to stay on the symmetry plane and off-center from the Sr site both in the ground state and in the two first excited states. The ground state cluster structure is shown in Fig. 5   In it, one oxygen atom in the σ_{yz} symmetry plane at 2.79 Å from Bi, O_a, and four sets of two off-plane symmetry related oxygen atoms: two at 2.39 Å, O_b, two at 2.60 Å, O_c, two at 2.81 Å, O_d, and two at 3.02 Å, O_e.
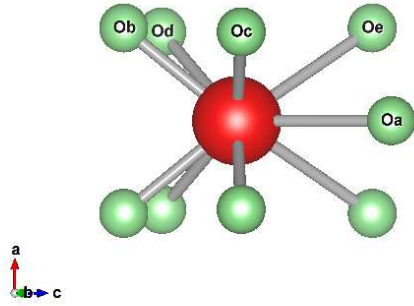
field in three states spanning more than 12000 cm^{-1}. The

FIG. 5: BiO$_9$ moiety. The *a*, *b*, and *c* axes of the SrB$_4$O$_7$ orthorhombic lattice are shown. O$_a$ is in the symmetry plane, which is perpendicular to the *a* axis; O$_b$, O$_c$, O$_d$, and O$_e$ are out of plane and their symmetry related oxygens are unlabelled. The Bi-O distances in the unrelaxed host and in the ground state relaxed host (in parenthesis) are, in Å: Bi-O$_a$ 2.73(2.79), Bi-O$_b$ 2.47(2.39), Bi-O$_c$ 2.68(2.60), Bi-O$_d$ 2.79(2.81), and Bi-O$_e$ 2.90(3.02).

1. Spin-orbit coupling free states.

Although the spin-orbit coupling splitting of the 6*p* shell of bismuth is so large that the electronic structure of Bi^{2+} in SrB$_4$O$_7$ can only be understood at the spin-orbit coupling level, it is convenient to describe firstly the electronic states of the spin-orbit coupling free Hamiltonian and later those of the full Hamiltonian in order to get insight. We summarize the spin-orbit free calculations in Table III.

TABLE III: Lowest energy levels of the (BiO$_9$)$^{16-}$ cluster embedded in SrB$_4$O$_7$ calculated without spin-orbit coupling (MS-CASPT2 level of theory). Point symmetry is $C_s(yz)$. Energies in cm^{-1}. Natural orbital main characters and occupations are shown. The NO's are represented in Fig. 6; see Ref. 45 for an interactive representation. They are provided in the Supplementary Material.

Energy	Level	Configurational character
0	1 $^2A''$	$a'(6s)^{1.98}$ $a''(6p_x)^{0.99}$
4070	1 $^2A'$	$a'(6s)^{1.98}$ $a'(6p_y)^{0.99}$
12450	2 $^2A'$	$a'(6s)^{1.98}$ $a'(6p_z)^{0.99}$
49940	1 $^4A''$	$a'(6s)^{1.00}$ $a''(6p_x)^{1.00}$ $a'(6p_y)^{1.00}$
53760	3 $^2A'$	$a'(6s)^{1.10}$ $a''(6p_x)^{1.64}$ $(2_aa')^{0.13}$ $(3_aa')^{0.11}$ [a]
53810	2 $^2A''$	dominant $6s6p^2$
54490	4 $^2A'$	dominant $6s6p^2$
58320	2 $^4A''$	$a'(6s)^{1.00}$ $a''(6p_x)^{1.00}$ $a'(6p_z)^{1.00}$
61310	5 $^2A'$	dominant $6s6p^2$
62640	1 $^4A'$	$a'(6s)^{1.00}$ $a'(6p_y)^{1.00}$ $a'(6p_z)^{1.00}$

^{a}2$_a$a$'$ and 3$_a$a$'$ are the second and third active a' NOs (with occupations lower than 2) of the 3 $^2A'$ state; both of them are mainly mixtures of 6p_y, 6p_z, 6$d_{3x^2-r^2}$, and 6s.

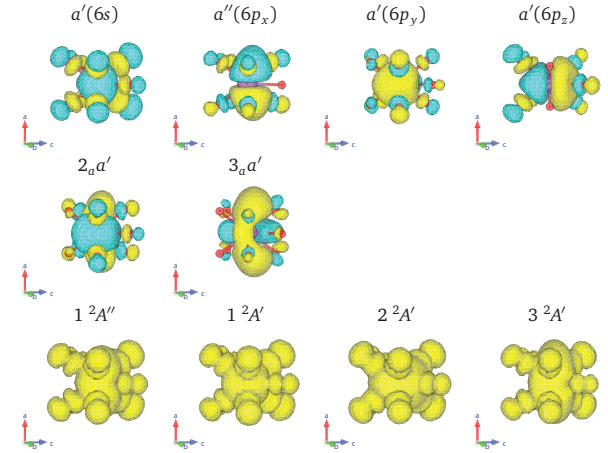The 6$s^2$6p $-^2P^o$ atomic term splits under the C_s effective

FIG. 6: Active natural orbitals (rows 1 and 2) and electron densities (row 3) of the spin-orbit free states (MS-CASPT2 calculations). See Table III. Note that there are small differences between the NOs $a'(6s)$, $a''(6p_x)$, $a'(6p_y)$, and $a'(6p_z)$ of different states, which are not visible in the scale of the figure.

interaction with higher atomic states is very small and the three states have a highly dominant 6$s^2$6p configurational character, as it can be seen in the natural orbital (NO) populations. The shapes of the $a'(6s)$, $a''(6p_x)$, $a'(6p_y)$, and $a'(6p_z)$ NOs are shown in the first row of Fig. 6 (cf. Ref. 45 for an interactive representation). The nodal planes between the oxygens and bismuth reveal the ionic character of their bonding interactions. The ground state is 1$^2A''$ and it has the 6p electron in the $a''(6p_x)$ antisymmetric orbital, which points perpendicular to the σ_{yz} symmetry plane in a direction between the four O$_b$, O$_c$, O$_d$, and O$_e$ atoms each side of the plane, with lowest electrostatic repulsion with them. This orbital has a nonbonding character with the in-plane O$_a$ atom. The first excited state is 1$^2A'$ and it has the 6p electron in the $a'(6p_y)$ symmetric orbital, with two nonequivalent lobes, the biggest one pointing towards the empty space between four oxygens (2 O$_d$ and 2 O$_e$) and the smallest one towards the mid point between the two O$_c$ atoms. Since this orientation is more repulsive than that of $a''(6p_x)$, 1$^2A'$ is above 1$^2A''$ in energy. The $a'(6p_y)$ NO has an almost nonbonding character with the two O$_b$ atoms, which lie very close to its nodal plane. The second excited state is 2$^2A'$ and it has the 6p electron in the $a'(6p_z)$ symmetric orbital, also with two nonequivalent lobes, the biggest one pointing towards the in-plane O$_a$ atom and the smallest one towards the mid point between the two O$_b$ atoms. This orientation is significantly more repulsive than the previous ones and, as a consequence, the 2$^2A'$ state lies at a significantly larger energy. The $a'(6p_z)$ NO has nonbonding character with the two O$_c$ atoms, which lie in its nodal plane.

The lowest state of the C_s splitting of the 6s6p^2 $-^4P$ atomic term is the third excited state, 1$^4A''$. It has an almost pure $a'(6s)a''(6p_x)a'(6p_y)$ configurational character, with the two 6p electrons occupying the two most stable

C_s-split $6p$ orbitals. The $6s \rightarrow 6p$ excitation implicit in this state makes it to appear more than 35000 cm^{-1} above the highest $^2P^o$ related state.

A group of states starts at about 4000 cm^{-1} above the latter, the lowest one lying 53760 cm^{-1} above the $1\,^2A''$ ground state and having a strong mixture of $6s6p^2$, $6s^26d$, and $6s^27p$ configurations. Its natural orbital occupations are $a'(6s)^{1.10}$ $a''(6p_x)^{1.64}$ $(2_a a')^{0.13}$ $(3_a a')^{0.11}$; the populations of $a'(6s)$ and $a''(6p_x)$ indicate the strong configurational mixing and the second and third active a' NOs, $2_a a'$ and $3_a a'$, which allocate together 0.25 electrons, are mainly mixtures of $6p_y$, $6p_z$, $6d_{3x^2-r^2}$, and $6s$. They are shown in the second row in Fig. 6. We did not see significant contributions from the $6s^27s$ configuration up to

70000 cm^{-1}; let us remind that $6s^27s$-$^2S_{1/2}$ has been assumed to be the third excited state.[1,5,7]

2. *States including spin-orbit coupling.*

All the states of the full Hamiltonian are Kramers doublets that belong to the $E_{1/2}$ irreducible representation of the C_s' double group. The relative energies and spin-orbit free characters of the lowest states computed with the ground state equilibrium structure are shown in Table IV, together with the absorption oscillator strengths.

TABLE IV: Lowest $E_{1/2}$ Kramers doublets of $(BiO_9)^{16-}$ embedded in SrB_4O_7 (C_s' double group) computed at the ground state structure using the spin-orbit coupling Hamiltonian (RASSI-SO level of theory). Energies relative to the ground state (cm^{-1}), absorption oscillator strenghts, and analysis of the wave functions in terms of their spin-orbit free characters (contributions larger than 5% are given).

State	Energy	f_{abs}	Percentage contributions of spin-orbit free states			
$1\,E_{1/2}$	0		53.9 $1\,^2A''$	31.4 $1\,^2A'$	14.5 $2\,^2A'$	
$2\,E_{1/2}$	14450	4.2×10^{-4}	55.7 $1\,^2A'$	42.0 $1\,^2A''$		
$3\,E_{1/2}$	21830	1.1×10^{-3}	83.0 $2\,^2A'$	12.8 $1\,^2A'$		
$4\,E_{1/2}$	47260	1.3×10^{-1}	39.5 $1\,^4A''$	15.2 $2\,^4A''$	10.7 $3\,^2A'$	8.4 $1\,^4A'$
			8.4 $5\,^2A'$	7.8 $2\,^2A''$		
$5\,E_{1/2}$	56070	3.7×10^{-3}	85.1 $1\,^4A''$	6.2 $2\,^4A''$		
$6\,E_{1/2}$	59520	2.6×10^{-1}	54.4 $2\,^2A''$	23.2 $1\,^4A''$	9.5 $2\,^4A''$	5.0 $5\,^2A''$

The spin-orbit coupling interactions between the three lowest spin-orbit free states, all of them of $6s^26p$-$^2P^o$ character, dominate the three lowest $E_{1/2}$ states. The contributions from higher spin-orbit free states are indeed very small. In Fig. 7, we present a quantitative diagram of the 1-3 $E_{1/2}$ energy levels together with the spin-orbit free counterparts $1\,^2A''$, $1\,^2A'$, and $2\,^2A'$ and the computed free-ion levels $^2P_{1/2}$ and $^2P_{3/2}$. We show all of them in a common energy scale in which their respective averages and the Bi^{2+} free-ion spin-orbit coupling free term ^2P are set to zero (left scale). In this scale, the difference between $1E_{1/2}$ and $^2P_{1/2}$ is 450 cm^{-1}, and the difference between the average energy of $2E_{1/2}$ and $3E_{1/2}$ and $^2P_{3/2}$ is -220 cm^{-1}. This shows the very small influence of excited configurations on the $6s^26p$-^2P related states. In black dashed lines, we show the theoretical results of using state average weights 1 and 4 for the $6s^26p -^2P$ and $6s^27p -^2P$ states in the SA-CASSCF step of the calculations of Bi^{2+} free-ion. This result agrees very well with the experiment shown in red dashed lines. Such an agreement is due to the fact that this state-averaging corrects the deficiencies of the spin-orbit coupling, cf. Sec. V B. However, we cannot use these

state average weights in our $(BiO_9)^{16-}$ embedded cluster calculation because the states related with the $6s^27p$ configuration are very high in energy. So, according to this result, we must expect our calculation to underestimate the average energy of the two first excited states with respect to the ground state.

The third excited state $4E_{1/2}$, which is assumed to have a $6s^27s -^2S_{1/2}$ main character in the literature,[1,5,7–11] has a 63% character of $6s6p^2 -^4P$. The rest of its character is spread over several doublets of $6s6p^2$, $6s^26d$, and $6s^27p$ configurations, with no sign of relevant $6s^27s$ character. The larger value of the absorption oscillator strength from the ground state to $4E_{1/2}$ with respect to the previous two excited states must be associated, then, to the partial $6s \rightarrow 6p$ and $6p \rightarrow 6d$ characters involved in the $1E_{1/2} \rightarrow 4E_{1/2}$ absorption.

The computed radiative lifetime of the $2E_{1/2}$ state, which is responsible for the red-orange emission, is $\tau_{0,rad} =17$ μs *in vacuo*. After including standard local field corrections[46] calculated with a refraction index of SrB_4O_7 $n=1.74$ (Ref. 47) the lifetime in the solid is 3.5 μs. This means a local field reduction by a factor of 4.9. Lifetimes of other ex-
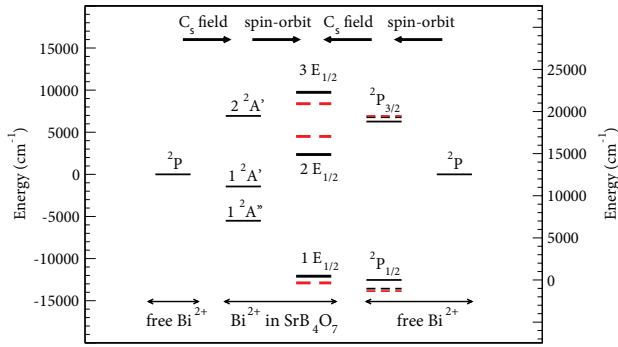
FIG. 7: Quantitative correlation level diagram. Black lines: *ab initio* calculations; free-ion results using 1-4 state-average weights (last column in Table II) are shown in dashed lines. Red dashed lines: experiments. See text for details.

cited states computed with the same correction are shown in Fig. 8.

D. Comparisons with experiments

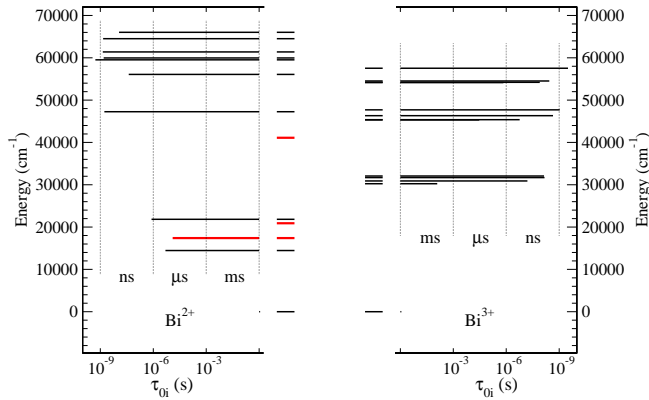The comparisons between the *ab initio* calculations and experimental data are summarized in Table V and Fig. 8.

FIG. 8: Energy levels and radiative lifetimes of the states of Bi^{2+} and Bi^{3+} in SrB_4O_7. Black: *ab initio* calculations. Red: experimental results attributed to the Bi^{2+} defect.

The pattern of excited states agrees with the experimental excitation spectra: two states in the 20000 cm^{-1} region of comparable excitation intensities and no other state up to the 40000 cm^{-1} region, where there is a third excitation of higher intensity. The data in Table V show a 2875 cm^{-1} underestimation of the first excited state $2E_{1/2}[^2P_{3/2}(1)]$ and 885 cm^{-1} overestimation of the second, $3E_{1/2}[^2P_{3/2}(2)]$. We can take the average of these two states as the spin-orbit splitting of Bi^{2+} ^2P in the host and their difference as a measure of the C_s field splitting. Then, we get a theoretical spin-orbit splitting of 17980 cm^{-1}, which is 95% of the experimental 18975 cm^{-1}. The origin of this underestimation is the same as in free Bi^{2+},

TABLE V: Excitation maxima (max ↑), emission maxima (max ↓), zero-phonon lines (ZPL), spin-orbit coupling splittings, C_s field splittings, absorption oscillator strengths (f_{abs}), and radiative lifetimes. Energies in cm^{-1}.

		Experiment Energy	*Ab initio* Energy	f_{abs}
$1E_{1/2}[^2P^o_{1/2}]$		0	0	
$2E_{1/2}[^2P^o_{3/2}(1)]$	max ↑	17390[a]	14450	$4.2×10^{-4}$
		17300[b]		
	max ↓	17065[a]	14330	
		17000[b]		
	ZPL	17245[c]	14370	
$3E_{1/2}[^2P^o_{3/2}(2)]$	max ↑	21275[a]	21830	$1.1×10^{-3}$
		20900[b]		
	ZPL	20705[c]	21590	
$^2S_{1/2}(6s^27s)^d$	max ↑	>32000[a]		
		40800[b]		
$4E_{1/2}(6s6p^2,6s^26d,6s^27p)^e$		41100[c]	47260	$1.3×10^{-1}$
$^2P^o$ SO splitting		18975[c]	17980	
$^2P^o_{3/2}$ C_s splitting		3460[c]	7220	
$2E_{1/2}[^2P^o_{3/2}(1)]$ lifetime (μs)		10.2[a]	3.5	
		13.0[b]		
		12.6[c]		

[a]Reference 1.
[b]Reference 7.
[c]This work.
[d]Assignment of the third excitation band in References 1 and 7.
[e]Assignment of the third excitation band in this work .

where the theoretical spin-orbit splitting of the $^2P^o$ term at the same level of calculation was 91% of the experimental value (cf. Table II). As discussed in Sec. V B, the reason is that the two-step spin-orbit method used here uses few degrees of freedom to produce different radial functions for the $6p_{1/2}$ and $6p_{3/2}$ spinors and hence the underestimation. Whereas correcting this via state-average weights was possible in free Bi^{2+}, it is not in the $(BiO_9)^{16-}$ embedded cluster because the neccesary spin-orbit free states to be mixed are very high in energy. Concerning the C_s field splitting, the calculations overestimate that of $^2P_{3/2}$: 7220 cm^{-1} vs. 3460 cm^{-1}. This overestimation is consistent with the lack of lattice relaxation effects in the calculations because oxygen displacements away from the Bi^{2+} impurity would lower the splitting. It cannnot be ruled out that it is due in part to an overestimation of repulsive effects in the SrB_4O_7 embedding potential.

The computed absorption oscillator strengths of the second and third bands are 2.6 and 310 times larger than that of the first band. These values are different from the experimentally observed ratios of 0.98 and 1.38. Especially the high-energy band around 41000 cm^{-1} is weaker than

expected in the excitation spectrum. The low intensity can be due to direct non-radiative decay from this high-energy state to the ground state (not yielding emission) or, more likely, to competing absorption from defects or Bi^{3+} also not giving rise to the orange emission that is monitored in the excitation spectrum.

The 3.5 μs for the computed radiative lifetime of the emitting state $2E_{1/2}[^2P^o_{3/2}(1)]$ is not far from the experimental values, which range between 10 and 13 μs. In Fig. 8 we present a graphic comparison with the experiment and with radiative lifetimes of other states of Bi^{2+} and Bi^{3+} in SrB_4O_7. The energy levels and lifetimes of Bi^{3+} have been computed in calculations equivalent to the ones for Bi^{2+}, using the $(BiO_9)^{15-}$ embedded cluster. It is important to remark that the only states with a lifetime in the range of the experimental measurements are the $2E_{1/2}[^2P^o_{3/2}(1)]$ and $3E_{1/2}[^2P^o_{3/2}(2)]$ states of Bi^{2+}, the only possible emitting state being the first of them. The lowest set of states of Bi^{3+} has one state with a lifetime in the millisecond regime (corresponding to a $^3P_0 \rightarrow{}^1 S_0$ emission) and the others in the nanosecond regime (corresponding to $\mu^3P_1 + \nu^1P_1 \rightarrow{}^1 S_0$ emissions), as it is usually found in the luminescence of Bi^{3+} in solid hosts.[48,49] This, together with its higher energy, rules out the consideration of a state in this set as possible emitter.

The overall agreement between the *ab initio* calculations and the experimental optical measurements strongly supports the initial hypothesis of Blasse *et al.*[1] of stable Bi^{2+} species as responsible of the red-orange luminescence of bismuth-doped SrB_4O_7.

VI.   CONCLUSIONS

Low temperature luminescence experiments give the zero-phonon lines of the blue excitation and red-orange emission of bismuth-doped SrB_4O_7, which have been attributed to transitions between the $^2P_{1/2}$ ground state and the $^2P_{3/2}(1)$ and $^2P_{3/2}(2)$ excited states of Bi^{2+} in a low symmetry C_s site.[1] The influence of the Bi-concentration on the emission intensity is small and only a small increase of the red-orange emission is observed upon raising the nominal Bi concentration from 0.02% (200 ppm) to 2%. This result indicates that only a very low concentration of Bi^{2+} can be incorporated in SrB_4O_7. Its upper limit is estimated

to be 20 ppm. EPR measurements do not detect the presence of Bi^{2+} and XANES results suggest Bi^{3+} as the dominant species, both indicating that stable divalent bismuth could only be present in very low concentration, below detection limits for these techniques. Wave function based *ab initio* calculations on the $(BiO_9)^{16-}$ cluster embedded in SrB_4O_7 provide an independent, additional support to the interpretation of stable Bi^{2+} species as responsible for the red-orange luminescence of the material. The support is based on the agreement between calculated and experimental level energies and emitting state lifetime. Equivalent calculations for the Bi^{3+} species are very far from experiment.

The calculatons provide a new interpretation of the third excitation band, which is not due to a $^2S_{1/2}$ state of the $6s^27s$ configuration of Bi^{2+}, as previously assumed, but to a state with important characters of $6s6p^2 -{}^4 P$ (63%) and doublets of the $6s6p^2$, $6s^26d$, and $6s^26p$ configurations; its higher intensity is due to its character of parity allowed $6s \rightarrow 6p$ and $6p \rightarrow 6d$ excitations.

In summary, although EPR and XANES do not give a direct proof of the presence of Bi^{2+}, luminescence and *ab initio* results coincide on attributing the red-orange luminescence of bismuth-doped SrB_4O_7 to a stable Bi^{2+} species. The concentration of this species has a very low upper limit in the ppm range.

* Corresponding author; Electronic address: `luis.seijo@uam.es`
[1] G. Blasse, A. Meijerink, M. Nomes, and J. Zuidema, J. Phys. Chem. Solids **55**, 171 (1994).
[2] L. de Boisbaudran, C. R. Acad. Sci. Paris **103**, 629 (1886).
[3] F. A. Kröger, J. T. G. Overbeek, J. Goorissen, and J. van den Boomgaard, Trans Electrochem. Soc. **96**, 132 (1949).
[4] M. A. Hamstra, H. F. Folkerts, and G. Blasse, J. Mater. Chem. **4**, 1349 (1994).

[5] A. M. Srivastava, J. Lumin. **78**, 239 (1998).
[6] Q. Zeng, T. Zhang, Z. Pei, and Q. Su, J. Mater. Sci. Technol. **15**, 281 (1999).
[7] M. Peng and L. Wondraczek, Opt. Lett. **34**, 2885 (2009).
[8] M. Peng and L. Wondraczek, Opt. Lett. **35**, 2544 (2010).
[9] Z. Bai, M. Fujii, T. Hasegawa, S. Kitano, K. Imakita, M. Mizuhata, and S. Hayashi, Opt. Mater. **34**, 821 (2012).
[10] M. Peng, J. Lei, L. Li, L. Wondraczek, Q. Zhang, and J. Qiu, J. Mater. Chem. C **1**, 5303 (2013).

[11] R. Cao, F. Zhang, C. Liao, and J. Qiu, Opt. Express **21**, 15728 (2013).

[12] A. C. Barnes, C. Guo, and W. S. Howells, J. Phys.: Condens. Matter **6**, L467 (1994).

[13] E. Ahmed, D. Köhler, and M. Ruck, Z. Anorg. Allg. Chem. **635**, 297 (2009).

[14] T. Ressler, J. Synchrotron Rad. **5**, 118 (1998).

[15] D. A. McKeown, H. Gan, and I. L. Pegg, J. Nucl. Mater. **420**, 116 (2012).

[16] R. D. Shannon, Acta Cryst. A **32**, 751 (1976).

[17] H. J. Murphy, K. T. Stevens, N. Y. Garces, M. Moldovan, N. C. Giles, and L. E. Halliburton, Radiat. Eff. Defect. S. **149**, 273 (1999).

[18] G. Karlström, R. Lindh, P. A. Malmqvist, B. O. Roos, U. Ryde, V. Veryazov, P. O. Widmark, M. Cossi, B. Schimmelpfennig, P. Neogrady, and L. Seijo, Comput. Mater. Sci. **28**, 222 (2003).

[19] J. Krogh-Moe, Acta Chem. Scand. **18**, 2055 (1964).

[20] M. Douglas and N. M. Kroll, Ann. Phys. (N.Y.) **82**, 89 (1974).

[21] B. A. Hess, Phys. Rev. A **33**, 3742 (1986).

[22] B. O. Roos, P. R. Taylor, and P. E. M. Siegbahn, Chem. Phys. **48**, 157 (1980).

[23] P. E. M. Siegbahn, A. Heiberg, B. O. Roos, and B. Levy, Phys. Scr. **21**, 323 (1980).

[24] P. E. M. Siegbahn, A. Heiberg, J. Almlöf, and B. O. Roos, J. Chem. Phys. **74**, 2384 (1981).

[25] K. Andersson, P.-Å. Malmqvist, B. O. Roos, A. J. Sadlej, and K. Wolinski, J. Phys. Chem. **94**, 5483 (1990).

[26] K. Andersson, P.-Å. Malmqvist and B. O. Roos, J. Chem. Phys. **96**, 1218 (1992).

[27] A. Zaitsevskii and J. P. Malrieu, Chem. Phys. Lett. **233**, 597 (1995).

[28] J. Finley, P.-Å. Malmqvist, B. O. Roos and L. Serrano-Andrés, Chem. Phys. Lett. **288**, 299 (1998).

[29] G. Ghigo, B. O. Roos, and P.-Å. Malmqvist, Chem. Phys. Lett. **396**, 142 (2004).

[30] B. A. Hess, C. M. Marian, U. Wahlgren, and O. Gropen, Chem. Phys. Lett. **251**, 365 (1996).

[31] R. Llusar, M. Casarrubios, Z. Barandiarán, and L. Seijo, J. Chem. Phys. **105**, 5321 (1996).

[32] P. A. Malmqvist, B. O. Roos, and B. Schimmelpfennig, Chem. Phys. Lett. **357**, 230 (2002).

[33] J. Paulovic, T. Nakajima, K. Hirao, R. Lindh, , and P.-A. Malmqvist, J. Chem. Phys. **119**, 798 (2003).

[34] B. O. Roos, R. Lindh, P. A. Malmqvist, V. Veryazov, and P. O. Widmark, J. Chem. Phys. **108**, 2851 (2005).

[35] Z. Barandiarán and L. Seijo, J. Chem. Phys. **89**, 5739 (1988).

[36] Detailed embedding AIMP data libraries in electronic format are available from the authors upon request or directly at the address http://www.uam.es/quimica/aimp/-Data/AIMPLibs.html. See also Ref. 18.

[37] A. Gellé and M.-B. Lepetit, J. Chem. Phys. **128**, 244716 (2008).

[38] P. P. Ewald, Ann. Phys.-Paris **64**, 253 (1921).

[39] L. Seijo and Z. Barandiarán, J. Chem. Phys. **94**, 8158 (1991).

[40] NIST Atomic Spectra Database, NIST Standard Reference Database #78.

[41] T. Fleig, J. Olsen, and C. M. Marian, J. Chem. Phys. **114**, 4775 (2001).

[42] C. Froese-Fischer, *The Hartree-Fock method for atoms* (John Wiley, New York, 1977).

[43] T. H. Dunning, Jr., B. H. Botch and J. F. Harrison, J. Chem. Phys. **72**, 3419 (1980).

[44] M. de Jong, A. Meijerink, Z. Barandiarán, and L. Seijo, in preparation.

[45] Follow the address http://www.uam.es/departamentos/-ciencias/quimica/aimp/Data/MO/ for interactive MO representations.

[46] B. Henderson and G. F. Imbusch, *Optical spectroscopy of inorganic solids* (Clarendon Press, Oxford, 1989).

[47] F. Pan, G. Shen, R. Wang, X. Wang, and D. Shen, J. Cryst. Growth **241**, 108 (2002).

[48] A. Wolfert and G. Blasse, J. Solid State Chem. **59**, 133 (1985).

[49] A. Wolfert, E. W. J. L. Oomen, and G. Blasse, J. Solid State Chem. **59**, 280 (1985).